Optoelectronic Materials ISSN 2377-4738 *Optoelectron Mater.* ***1*** *(2016) 50–56*

Effect of post sintering temperature on the morphology and photoluminescence of co-precipitation derived $ZnMoO_4$ microcrystals

Bao-gai Zhai, Yuan Ming Huang*

[1]School of Mathematics and Physics, Changzhou University, Jiangsu 213164, China
(*Received 10 March 2016; accepted 6 July 2016*)

Triclinic zinc molybdenum tetraoxide ($ZnMoO_4$) microcrystals were synthesized by the co-precipitation method and subsequent sintering in air. The effects of sintering temperature on the morphology and photoluminescence (PL) of $ZnMoO_4$ microcrystals were investigated by means of by means of X-ray diffraction, scanning electron microscopy, transmission electron microscopy, UV-vis reflectance spectroscopy, and PL spectrophotometry. It is found that both the morphology and PL properties of $ZnMoO_4$ microcrystals are dependent on the sintering temperature of the precipitate. As the sintering temperature increases from 300 to 600ºC, the morphology of $ZnMoO_4$ changes from microspheres full of pores to well-developed microcrystals, and in the meanwhile the static PL spectrum of the sintered $ZnMoO_4$ exhibits a broad profile with its peak varying from 510 to 560 nm. The band structures and density of states of $ZnMoO_4$ are calculated with density functional theory in the frame of local density approximation. We have demonstrated that $ZnMoO_4$, which is an indirect semiconductor with the band gap of 3.7 eV, can find wide applications in luminescent materials.

Keywords: Zinc molybdenum oxide; Morphology; Static photoluminescence; Time-resolved photoluminescence; Density functional calculations; Electronic structures

1. Introduction

As a typical transition metal material, zinc molybdate tetraoxide ($ZnMoO_4$) are commonly applied as croyogenic photon-scintillation detectors in the search of double neutrinoless β-decay because zinc has no radioactive isotopes and, hence, does not produce any noise during signal recording [1-5]. $ZnMoO_4$ belongs to the wolframite-type metal molybdates with triclinic symmetry. In addition to the application as scintillation detectors, $ZnMoO_4$ has recently roused the attention of scientists because undoped $ZnMoO_4$ exhibits a high yield in photoluminescence (PL) whilst rare-earth doped $ZnMoO_4$ can give off tunable PL [6-10]. For example, it was reported that undoped $ZnMoO_4$ exhibits a broad band PL with a maximum at 1.95 eV (636 nm) [7,8] whereas Eu^{3+}, Dy^{3+} and Tb^{3+} doped $ZnMoO_4$ exhibits efficient red, white and green emissions, respectively [9-12]. Up to now, a variety of methods have been used to synthesize $ZnMoO_4$, examples include Czochralski technique [6,7], solid state reactions [9-11], precipitation and heat-treatment methods [12,13], hydrothermal methods [14,15], electrospinning method [16], microwave irradiation [17], and laser ablation in liquids [18]. Among these techniques, the method of co-precipitation and subsequent calcination at a specific temperature is a general precipitation strategy for large-scale synthesis of molybdate nanostructures [12,13], and it is expected that subsequent sintering temperature will generate significant effects on the morphology and luminescent properties of resulted $ZnMoO_4$. In order to synthesize $ZnMoO_4$ with desired morphology and luminescent properties, it is important to study the effects of the subsequent sintering temperature on the morphology and luminescent properties of $ZnMoO_4$. However, a brief literature survey indicates that the effects of the subsequent sintering temperature on the morphology and luminescent properties of $ZnMoO_4$ have not been investigated to date.

*Corresponding author. Email: dongshanisland@126.com

In this paper, $ZnMoO_4$ microcrystals were synthesized via the method of co-precipitation and subsequent calcination at temperatures in the range of 300 – 600º C. The purpose of this study is to investigate the effects of sintering temperature on the morphology and PL properties of $ZnMoO_4$.

2. Materials, characterizations and computation

The precursor of $ZnMoO_4$ was synthesized via the co-precipitation method using hexaammonium heptamolybdate tetrahydrate ($(NH_4)_6Mo_7O_{24}•4H_2O$) and zinc nitrate hexahydrate ($Zn(NO_3)_2•6H_2O$) as the starting materials. In three separated beakers, aqueous solutions A, B and C were prepared by dissolving $(NH_4)_6Mo_7O_{24}•4H_2O$ (0.01 mol), NaOH (0.08 mol) and $Zn(NO_3)_2•6H_2O$ (0.07 mol) into 100 ml deionized water, respectively. Under vigorous stirring with a magnetic bar, solution B was dropped into solution A to hydrolyze $(NH_4)_6Mo_7O_{24}$. Then solution C was gradually added to the hydrolyzed solution with the result of white precipitate. The precipitate was filtered, washed several times with distilled water and ethanol, and dried in an oven for overnight. The dried white powder served as the precursor of $ZnMoO_4$. Four types of $ZnMoO_4$ microcrystals were formed by subsequent sintering the precipitate in an air-filled furnace at 300, 400, 500 and 600 ºC for 2 h, respectively.

The scanning electron microscope (SEM) (S-4800, Hitachi, Japan) and X-ray diffractometer (XRD) (D/max 2500 PC, Japan) were employed to analyze the morphology and crystal structures of the synthesized $ZnMoO_4$ microcrystals. The PL spectra of $ZnMoO_4$ microcrystals were recorded with a spectrophotometer (Tianjin Gangdong Ltd., China). The 325-nm laser line from a helium-cadmium laser was utilized as the excitation source for the PL measurement. The PL lifetime measurement of $ZnMoO_4$ microcrystals was performed at room temperature on a picosecond fluorescence lifetime spectrometer (LifeSpec II,

Edinburgh Instruments). The 375 nm excitation source was supplied with a picosecond pulsed laser while the emission wavelength was 540 nm.

First-principles density functional theory (DFT) calculations of the band structures of $ZnMoO_4$ with various defects were performed using the DFT module of the Quantumwise Atomistix ToolKit 11.8 package. The exchange-correlation functional was treated within the LDA scheme, in which the exchange potential was parameterized by Perdew and Zunger. Triclinic $ZnMoO_4$ belongs to space group $P\bar{1}$. There were 6 Zn, 6 Mo and 24 O atoms in the unit cell of $ZnMoO_4$. The parameters of triclinic $ZnMoO_4$ were a = 0.9625 nm, b = 0.6965 nm, c = 0.8373 nm, α = 103.28, β = 96.30 and γ = 106.72°. The considered electronic configurations were $3d^{10}4s^24p^0$ for Zn, $2s^22p^4$ for O, $4p^64d^55s^1$ for Mo. Double zeta single polarized basis sets were chosen for each element. The electronic wavefunctions were expanded in plane waves up to a kinetic energy cut-off with a typical value of 100 Hartree. The Brillouin zone was sampled by a 5 × 5 × 5 Monkhorst-Pack mesh of k points. The Brillouin zone sampling and the kinetic energy cutoff were sufficient to guarantee an excellent convergence for the calculated band structures. The convergence tolerance of the calculation was 4×10^{-5} eV of the total energy.

3. Results and discussions

3.1 Morphology of $ZnMoO_4$ microcrystals

Fig. 1 shows SEM micrographs of $ZnMoO_4$ microcrystals grown by sintering the precipitate at different temperatures for 2 h: (a) 300°C; (b) 400°C; (c) 500°C; and (d) 600°C. After having been sintered at 300°C for 2h, $ZnMoO_4$ nanowires and microcrystals are formed, as shown in Fig. 1(a). In this study we focus on the $ZnMoO_4$ microcrystals only. On a whole, the $ZnMoO_4$ microcrystals are in the shape of spheres with a typical diameter of around 4 μm. Detailed analysis of Fig. 1(a) reveals that there are a lot of pores in the $ZnMoO_4$ microcrystals. As shown in Fig. 1(b), most of the $ZnMoO_4$ microcrystals keep their shape when the sintering temperature is 400°C. However, it is noted that some of the $ZnMoO_4$ microcrystals in Fig. 1(b) have cracks on the surface. When the sintering temperature is increased further to 500°C, all the $ZnMoO_4$ microspheres are broken into fragments. As shown in Fig. 1(c), the typical size of the $ZnMoO_4$ fragments is around 1 μm. when the sintering temperature is 600°C, as depicted in Fig. 1(d), the $ZnMoO_4$ fragments are developed into crystals with well-defined facets. Unlike the $ZnMoO_4$ microspheres full of pores in Fig. 1(a), the $ZnMoO_4$ microcrystals in Fig. 1(d) are free of any voids. It is worth noting that the melting temperature of $ZnMoO_4$ is 1003 ± 5°C and its melt crystallization temperature is 975 ± 5°C. So the crystals with well-defined facets in Fig. 1(d) suggests the existence of $ZnMoO_4$ vapor in the process of crystal growth. When compared to the polycrystalline $ZnMoO_4$ nanofibers synthesized via the electrospinning technique [16], the $ZnMoO_4$ microcrystals in Fig. 1(d) are single-crystalline in nature.

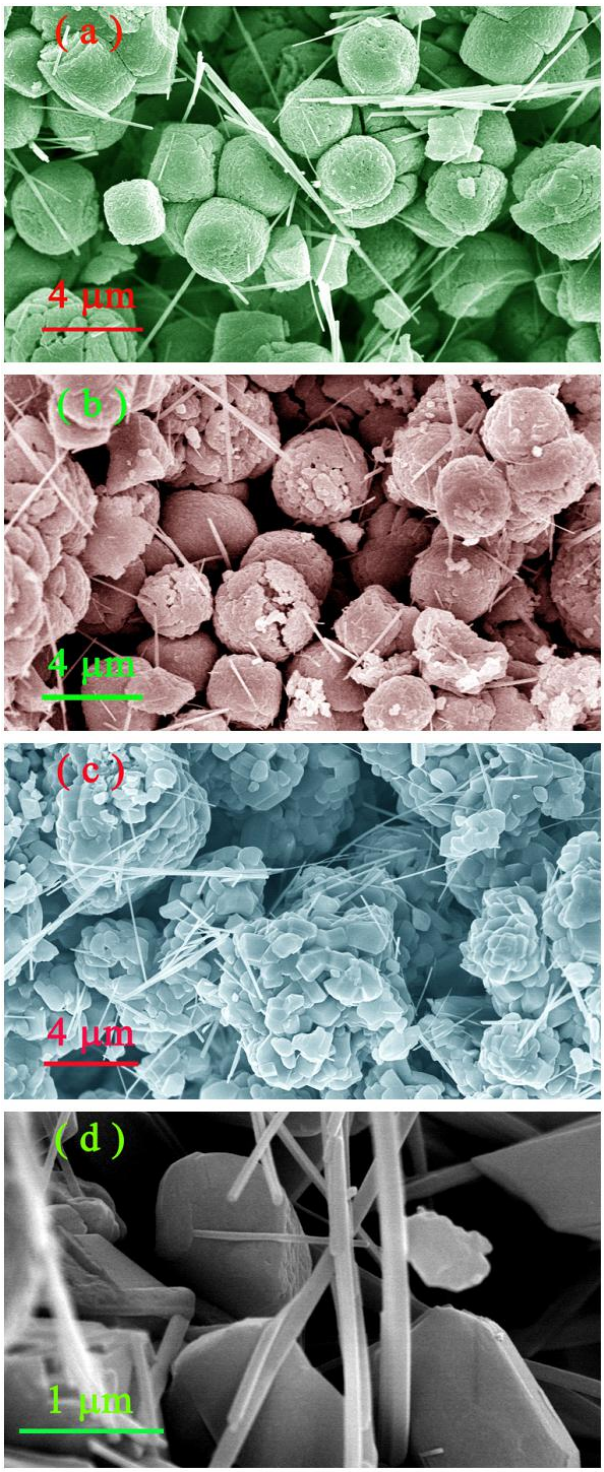

Fig. 1 SEM micrographs of $ZnMoO_4$ grown by sintering the precipitate at different temperatures for 2 h: (a) 300° C; (b) 400° C; (c) 500° C; and (d) 600° C.

Fig. 2 depicts the powder XRD curves of the ZnMoO4 microcrystals grown by sintering the precipitate at 300, 400, 500 and 600ºC for 2 h. It can be seen that diffraction peaks appear in each curve at 9.702, 13.219, 15.994, 19.235, 22.649, 24.179, 26.633, 27.597, 30.054, 33.388 and 33.876°, respectively. As discussed in our previous work, these eleven peaks can be assigned to the reflections from the 010, $\bar{1}10$, 110, 011, $1\bar{2}1$, 120, $\bar{2}20$, $2\bar{1}1$, $2\bar{2}1$, 300 and $\bar{2}12$ planes of the triclinic ZnMoO4 (JCPDS No.35–0765). Therefore, Fig. 2 has confirmed

that the $ZnMoO_4$ microcrystals are resulted via the co-precipitation and subsequent sintering approach. ZnMoO4 studied in this paper belongs to the α-ZnMoO4 structural type, space group $P\bar{1}$, triclinic system. The unit cell is composed of six $ZnMoO_4$ molecules. The lattice constants are a = 0.9625 nm, b = 0.6965 nm, c = 0.8373 nm, α = 103.28°, β = 96.30°, γ = 106.72°. In crystal structure, [MoO_4^{2-}] oxyanion complex is the principal constitutive element and plays a decisive role in its electronic structures and optical properties. The Mo atoms are surrounded by distorted oxygen tetrahedra creating three different types of MoO_4 complexes, and in the meanwhile Zn atoms are embedded into the octahedral Zn and pentahedral Zn positions [19].

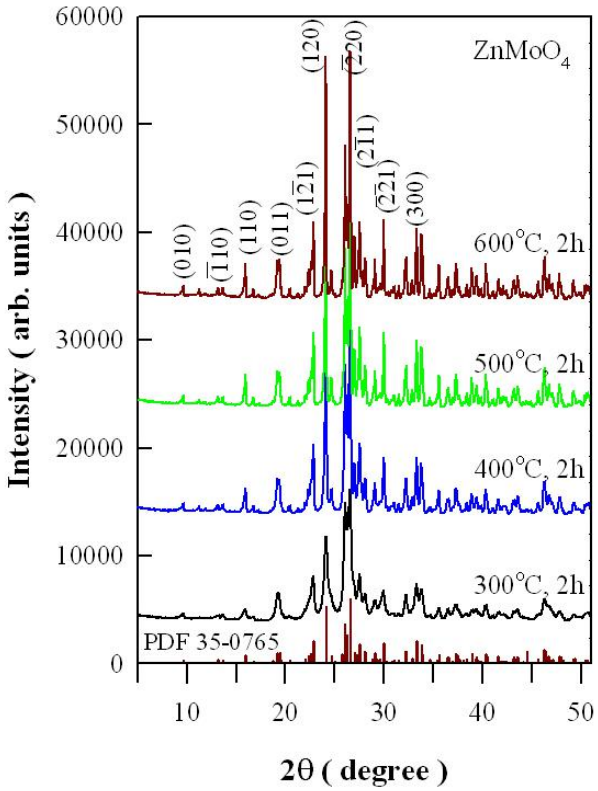

Fig. 2 XRD curves of the triclinic $ZnMoO_4$ grown by sintering the precipitate at 300, 400, 500 and 600° C for 2 h.

3.2 Reflectance and absorption spectra of $ZnMoO_4$

The optical absorption of $ZnMoO_4$ microcrystals was measured by diffuse reflectance spectroscopy at room temperature. Fig. 3(a) shows the typical diffuse reflectance spectrum of $ZnMoO_4$ microcrystals grown by sintering the precipitate at 500°C for 2 h. It can be seen that there is a strong absorption when the wavelength of incident photons is less than 375 nm. The absorption coefficient of the material can be derived from the reflectance spectrum by using the Kubelka-Munk function. This methodology is based on the transformation of diffuse reflectance measurements to estimate band gap values with good accuracy within the limits of assumptions when modeled in three dimensions. The Kubelka–Munk equation for any wavelength is

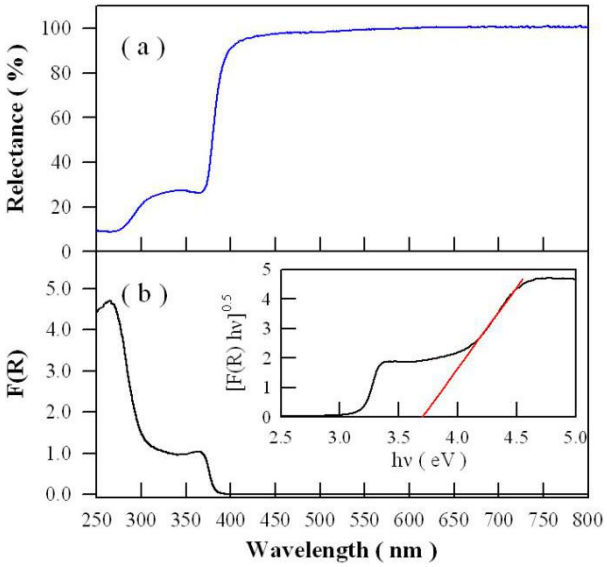

Fig. 3 Reflectance spectrum (a) and absorption spectrum (b) of $ZnMoO_4$ microcrystal grown at 500°C for 2 h.

described by Eq. (1):

$$F(R_\infty) = \frac{(1-R_\infty)^2}{2R_\infty} = \frac{k}{s} \quad (1)$$

where $F(R_\infty)$ is the Kubelka–Munk function of the sample, k is the molar absorption coefficient and s is the scattering coefficient. R_∞ is defined as the reflectance ration of the sample under test to the reference sample when the sample is infinitely thick. In our case, $BaSO_4$ was the standard sample in reflectance measurements. It can be seen from Eq. (1) that the absorption coefficient α of the material is directly proportion to $F(R_\infty)$. Fig. 3(b) shows the Kubelka–Munk function of the sample. It is clear that two absorption bands are present in Fig. 3(b), among which one starts its absorption at around 390 nm while the other starts its absorption at around 310 nm. When compared to the transmission spectrum of single crystal $ZnMoO_4$ [4,6], we can assign the strong absorption band in the range of 310-390 nm to defects in $ZnMoO_4$ microcrystals. In a parabolic band structure, the optical band gap and absorption coefficient of semiconductor oxides can be calculated by Eq. (2):

$$\alpha h\nu = C_1(h\nu - E_g)^n \quad (2)$$

where α is the linear absorption coefficient of the material, hν is the photon energy, C_1 is a proportionality constant, E_g is the optical band gap and n is a constant associated with different kinds of electronic transitions (n = 0.5 for a direct allowed, n = 2 for an indirect allowed, n = 1.5 for a direct forbidden and n = 3 for an indirect forbidden). According to the report in literature [19], triclinic $ZnMoO_4$ crystals is an indirect semiconductor. Based on this information, the E_g value of triclinic ZnMoO4 microcrystals can be calculated using n = 2 in Eq. (2). Finally, using the function described in Eq. (1), we obtain the modified Kubelka–Munk equation as indicated in Eq. (3):

$$[F(R_\infty)h\nu]^{0.5} = C_2(h\nu - E_g) \quad (3)$$

where $F(R_\infty)$ is directly proportion to the absorption coefficient α, C_2 is the characteristic constant of semiconductors, hν and Eg are the photon energy and optical band gap energy, respectively. The inset of Fig. 3(b) shows the the plot of $[F(R_\infty)hv]^{0.5}$ against hν for $ZnMoO_4$ microcrystals. The optical band gap energy, E_g, of $ZnMoO_4$ microcrystals was calculated to be 3.70 eV, which agrees well to the theoretically calculated band gap value of 3.79 eV [14]. Consequently, the intense absorption in Fig. 3(b) at around 310 nm is originated from electron transition from the valence band to the conduction of the $ZnMoO_4$ microcrystals.

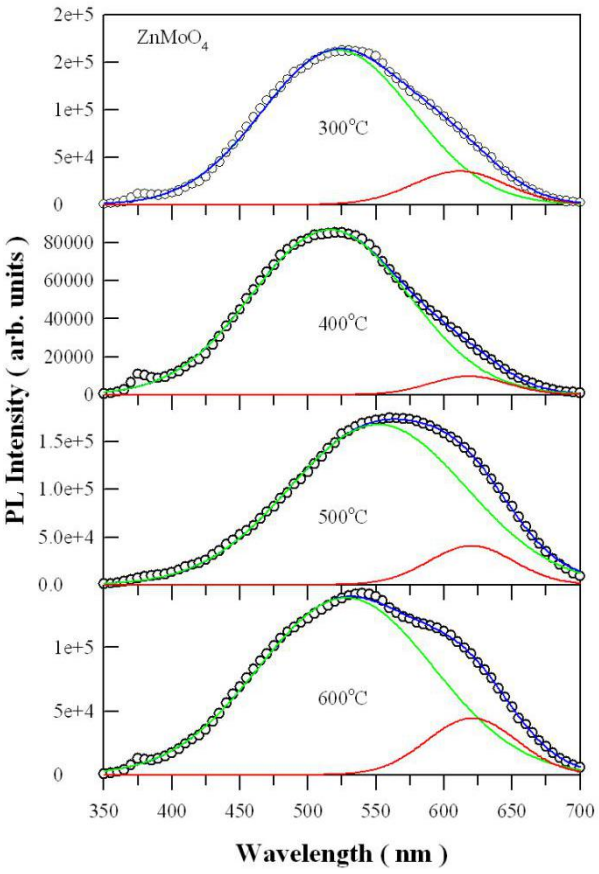

Fig. 4 PL spectra of $ZnMoO_4$ microcrystals grown by sintering the precipitate at 300, 400, 500 and 600°C for 2 h. The excitation wavelength was 325 nm.

3.3 PL spectra of $ZnMoO_4$ microcrystals

Upon photoexcitation, electrons and holes are created in the conduction and valence bands of the $ZnMoO_4$ microcrystals. Then the photoexcited carriers are relaxed through the near band edge free excitonic recombination and the intrinsic defects in the $ZnMoO_4$ microcrystals. Fig. 4 represents the PL spectra of $ZnMoO_4$ microcrystals grown by sintering the precipitate at 300, 400, 500 and 600° C for 2 h. It is clear that each PL spectrum in Fig. 4 is broad in profile. The peak position of the PL spectrum varies from 510 to 560 nm, depending on the sintering temperature. In order to investigate the effect of sintering temperature on the PL of $ZnMoO_4$ microcrystals, we decomposed each of the broad PL spectrum in Fig. 4 into two Gaussian components according the following equation

$$I = I_1 \exp\left[-\frac{(x-x_1)^2}{2b_1^2}\right] + I_2 \exp\left[-\frac{(x-x_2)^2}{2b_2^2}\right] \qquad (4)$$

where I is the total PL intensity, I_1 and I_2 are the PL intensities of the two components, x_1 and x_2 are the peak positions of the two components. Circles in Fig. 4 represent the experimental data, the pink curve in Fig. 4 represents the sum of the two components. The results of two-component Gaussian decomposition of the PL spectra are listed in Table 1 for $ZnMoO_4$ microcrystals grown at different temperatures. Additionally. the multiple correlation coefficient (R) and the coefficient of determination (R^2) of the curve fitting are listed in Table 1 for the evaluation of the fitting efficiency. It is clear that the peaks of green PL components are located at 521.66, 516.14, 551.45 and 528.01 nm when the sintering temperatures are 300, 400, 500 and 600°C, respectively. In contrast to the random change in the peak position of the green PL component, the peaks of red PL components, which are located at 611.24, 617.85, 619.99 and 620.47 nm when the sintering temperature are 300, 400, 500 and 600°C, increase monotonically with the sintering temperatures. In particular, the red PL band increases in intensity with the sintering temperature.

Table 1. Parameters of two-component Gaussian decomposition of the PL spectra for the $ZnMoO_4$ grown at different sintering temperatures and the multiple correlation coefficient (R) and the coefficient of determination (R^2) of the curve fitting.

	300°C	400°C	500°C	600°C
I_1	162822.2	86736.6	167856.5	138888.9
x_1	521.66	516.14	551.45	528.01
b_1	55.37	57.70	65.04	64.41
I_2	35264.7	9700.3	40780.3	44445.1
x_2	611.24	617.85	619.99	620.47
b_2	34.60	28.70	31.51	33.34
R	0.9989	0.9987	0.9994	0.9991
R^2	0.9978	0.9974	0.9987	0.9981

We have noticed that the PL spectra of the $ZnMoO_4$ microcrystals in Fig. 4 are quite different from those from $ZnMoO_4$ single crystals [6,7], nanofibers [16] and nanocrystals [17]. For instance, Spassky *et al.* observed two overlapping luminescence bands with the maxima 1.93 eV (643 nm) and 2.45 eV (506 nm) when measured at 7 K [6]; Mikhailik *et al.* reported that $ZnMoO_4$ exhibits a broad band PL with a maximum at 1.95 eV (636 nm) when measured at 78 K [7]; the PL peaks of $ZnMoO_4$ nanofibers and nanocrystals, on the contrary, were reported at around 400 nm [16,17]. As reported in the literature, the observed luminescence in $ZnMoO_4$ was attributed to the self-trapped exciton at MoO_4 complex, that is, the radiative recombination of electron-hole pair localized at the MoO_4 tetrahedrons. In order to make assignment of the main features in the PL spectrum of $ZnMoO_4$, it is useful to compare the peculiarities of the PL spectra in Fig. 4 to those of ZnO. A brief comparison

reveals that: (i) the broad PL band of $ZnMoO_4$ microcrystals resembles that of ZnO [21-24]; (ii) it has been known for a long time that $ZnMoO_4$ is the double oxides of the form $ZnO•MoO_3$, i.e. $ZnMoO_4$ can be regarded as the eutectic mixture of two-component $ZnO•MoO_3$ system [25]. Combination the results in Fig. 3 and Fig. 4 allows us to suggest that the PL in Fig. 4 can be attributed to defects in $ZnMoO_4$. Examples of the intrinsic defects in $ZnMoO_4$ include the oxygen vacancies, zinc vacancies, oxygen interstitials, zinc interstitials, oxygen antisites and zinc antisites. Here we do not consider the Zn and O antisites since their formation energies are usually high. Due to the lack of theoretical studies on the defects in $ZnMoO_4$, the correlation between the intrinsic defects in $ZnMoO_4$ and the recorded PL bands is still unclear, leaving the origin of the green PL band open to question. No matter which kind of defect is responsible for the green PL band, it is safe for us to conclude that the intense green PL band in Fig. 4 indicates the presence of sufficient amount of defects in the $ZnMoO_4$ microcrystals.

3.4 Time-resolved PL of $ZnMoO_4$ microcrystals

The PL decay time spectrum of $ZnMoO_4$ microcrystals, which were grown by sintering the precipitate at 500°C for 2 h, was measured at room temperature. Fig. 5 depicts the semi-logarithmic plot of the PL decay curve of $ZnMoO_4$ microcrystals under the excitation of 375 nm. The emission wavelength was fixed at 540 nm. The PL decay profile exhibits double exponential nature. The best fit to the experimental data was obtained using two exponentials with the decay time constants $\tau_1 = 0.93 \pm 0.02$ ns and $\tau_2 = 5.40 \pm 0.21$ ns for the PL emission at 540 nm. It is noted that $\tau 1$ is at the limit of the measurement capabilities of the instrument and therefore it merely represents the order of the short decay time constant. When compared to the long PL lifetime (3.9 μs) of the $ZnMoO_4$ single crystals grown by the Czochralski method [7], the observation of the quite short PL decay time gives further evidence on the defects in $ZnMoO_4$ microcrystals.

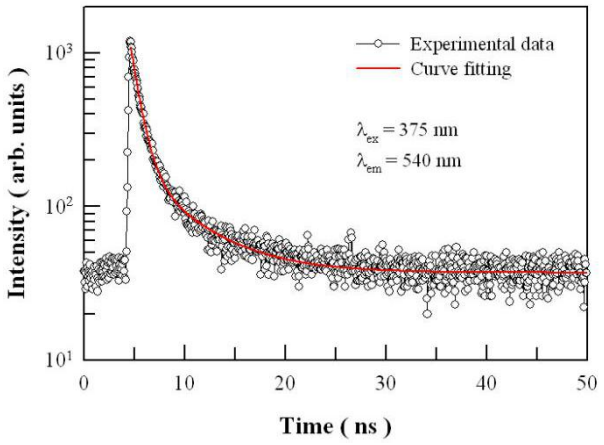

Fig. 5 Time-resolved PL spectra of $ZnMoO_4$ grown by sintering the precipitate at 500°C for 2 h.

3.5 Band structures of defect-free $ZnMoO_4$

A better insight into the origin of the PL properties of $ZnMoO_4$ can be gained by using the DFT based first-principles calculations. Fig. 6 illustrates the calculated band structures of defect-free triclinic $ZnMoO_4$. One-electron bands are in general uniformly distributed along the valence band (VB), excluding the region between -3 and -1.5 eV, where they are packed a little bit sparsely. As follows from the DFT calculations, the conduction band (CB) minimum (3.46 eV) is reached at the X point, the VB maximum (0 eV) can be found in the R point. Therefore, triclinic $ZnMoO_4$ crystal can be considered as an indirect gap material whose calculated band gap value equals 3.46 eV. When compared to the band gap value calculated by Spassky *et al* [19], our calculated value is only 0.3 eV lower. It should be noted that the band gap value obtained directly from our calculations should be somewhat corrected using experimental data. It is known that the band gap of a crystal may be underestimated if calculations are made under the DFT formalism. To overcome this drawback, the correcting energy addition to band gap or the 'scissor operator' is introduced at the stage of calculation to obtain the best fit between the calculated optical spectra and the corresponding experimental data. Another feature in Fig. 6 is the existence of two regions of relatively high density of states (3.5-4.5 eV and 4.7-6.7 eV) in the CB of $ZnMoO_4$. As Fig. 6 shows, these two regions contain dense groups of one-electron bands with a relatively low dispersion, which are separated by about 0.3 eV gap with zero density. One-electron bands are distributed more sparsely in the upper part of the CB. The splitting between these subbands corresponds to the E-T splitting of Mo 4d states in the tetrahedral crystal field.

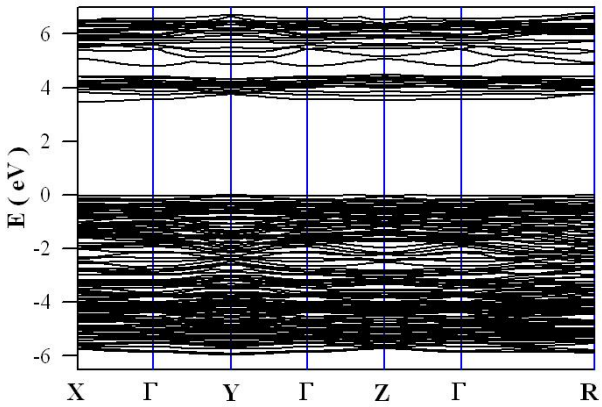

Fig. 6 Calculated band structures and density of states of defect-free triclinic $ZnMoO_4$.

The calculated total density of states (DOS) and partial DOS of $ZnMoO_4$ are presented in Fig. 7. The origin of the energy scale is chosen at the top of the valence band. A comparison of the four panels in Fig. 7 indicates that the Zn 3d, Mo 4d and O 2p states form the VB of the crystal which ranges from -6.0 to 0 eV. As a contrast, the contribution of the other types of electronic states (i.e., Mo 4p, Mo 5s, Zn 4s, Zn 4p and O 2s) to the VB is insignificant. In particular, the O 2s core band contributes nothing to VB since it is located 10 eV far below the bottom of the VB. As for the top of the VB, it is formed by O 2p and Zn 3d states without significant contribution from Mo 4d states. It is clear that $ZnMoO_4$ crystals are characteristic of the absence of Mo states at the top of the VB. The contribution of Zn 3d states increases in the

lower part of the VB. Now we come back to CB. As shown in the bottom panel, the Mo 4d states clearly dominate in the CB below 4.8 eV although O 2p and Zn 4s states contribute some to CB. Additionally, the Zn 3d states are practically absent in the CB. The calculated electronic structures can shed some insight on the origin of the PL from $ZnMoO_4$ microcrystals. For instance, it can be ensured that the PL in Fig. 4 originates from defect emissions in $ZnMoO_4$, instead of band-edge emission.

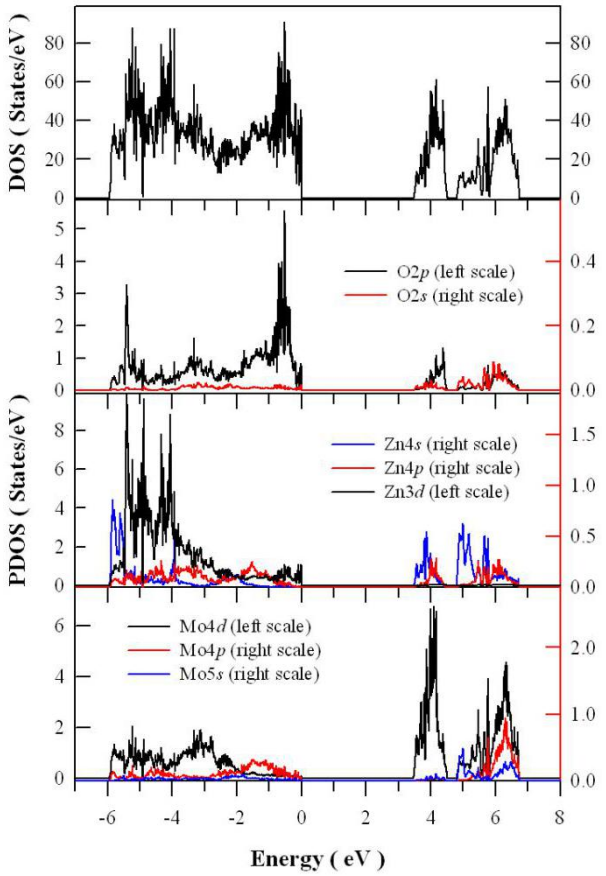

Fig. 7 Top panel: calculated total density of states of defect-free triclinic $ZnMoO_4$. The rest three panels: calculated partial density of states of defect-free triclinic $ZnMoO_4$.

4. Conclusions

Triclinic $ZnMoO_4$ microcrystals are synthesized by co-precipitation and subsequent sintering in air at 300, 400, 500 and 600°C for 2 h. The effects of sintering temperature on the morphology and PL properties of $ZnMoO_4$ microcrystals have been investigated by means of XRD, SEM, UV-vis reflectance spectroscopy and PL spectrophotometry. It is found that the morphology of the resulted $ZnMoO_4$ microcrystals are dependent on the sintering temperature. As the sintering temperature increases from 300 to 600° C, the morphology of $ZnMoO_4$ evolves from microspheres into broken fragments and eventually to microcrystals with well-defined facets. In the meanwhile the static PL spectrum of the synthesized $ZnMoO_4$ microcrystals exhibits a broad profile with its center varying from 510 to 560 nm. Each of the PL spectrum can be decomposed into a green Gaussian component and a red one. Higher sintering temperature enhances the intensity of its red PL component. Results on the calculated electronic structures of $ZnMoO_4$ are presented and aimed at shedding light on the origin of PL from $ZnMoO_4$ microcrystals. It can be ensured that the recorded green PL originates from defects in $ZnMoO_4$.

Acknowledgment

This work was financially supported by Natural Science Foundation of China under the Grant Nos 11304025, 11574036 and 1604028.

References

[1] L. Giron, Scintillating bolometers for double beta decay search. *Nucl. Instrum. Methods A* 617 (2010) 478－481.

[2] L. Gironi, C. Arnaboldi, J.W. Beeman, O. Cremonesi, F.A. Danevich, V.Ya. Degoda, L.I. Ivleva, L.L. Nagornaya, M. Pavan, G. Pessina, S. Pirro, V.I. Tretyak, I.A. Tupitsyna, Performance of $ZnMoO_4$ crystal as cryogenic scintillating bolometer to search for double beta decay of molybdenum. *J. Instr.* 5 (2010) 11007.

[3] L.L. Nagornaya, F.A. Danevich, A.M. Dubovik, B.V. Grinyov, S. Henry, V. Kapustyanyk, H. Kraus, D.V. Poda, V.M. Kudovbenko, V.B. Mikhailik, M. Panasyuk, O.G. Polischuk, V. Rudyk, V. Tsybulskyi, I.A. Tupitsyna, Yu. Ya. Vostretsov, Tungstate and molybdate scintillators to search for dark matter and double beta decay. *IEEE Trans. Nucl. Sci.* 56 (2009) 2513－2518.

[4] D.M. Chernyak, F.A. Danevich, V.Ya. Degoda, I.M. Dmitruk, F. Ferri, E.N. Galashov, A. Giuliani, I.M. Ivanov, V.V. Kobychev, M. Mancuso, S. Marnieros, V.M. Mokina, C. Nones, E. Olivieri, G. Pessina, C. Rusconi, V.N. Shlegel, O.P. Stanovyi, M. Tenconi, V.I. Tretyak, I.A. Tupitsyna, Optical, luminescence and thermal properties of radiopure $ZnMoO_4$ crystals used in scintillating bolometers for double beta decay search. *Nucl. Instrum. Methods A* 729 (2013) 856－863.

[5] J.W. Beeman, F. Bellini, P. Benetti, L. Cardani, N. Casali, D. Chiesa, M. Clemenza, I. Dafinei, S. Di Domizio, F. Ferroni, A. Giachero, L. Gironi, A. Giuliani, C. Gotti, M. Maino, S. Nagorny, S. Nisi, C. Nones, F. Orio, L. Pattavina, G. Pessina, G. Piperno, S. Pirro, E. Previtali, C. Rusconi, M. Tenconi, C. Tomei, M. Vignati, Current status and future perspectives of the LUCIFER experiment. *Adv. High Energy Phys.* 2013 (2013) 237973.

[6] D. Spassky, A. Vasil'ev, I. Kamenskikh, V. Kolobanov, V. Mikhailin, A, Savon, L, Ivleva, I. Voronina, L, Berezovskaya, Luminescence investigation of zinc molybdate single crystals. *Phys. Status Solidi C* 206 (2009) 1579－1583.

[7] V.B. Mikhailik, H. Kraus, D. Wahl, H. Ehrenberg, M.S. Mykhaylyk, Optical and luminescence studies of $ZnMoO_4$ using vacuum ultraviolet synchrotron radiation. *Nucl. Instrum. Methods A* 562 (2006) 513－516.

[8] D.A. Spassky, V.V. Mikhailin, A.E. Savon, E.N. Galashov, V.N. Shlegel, Ya.V. Vasiliev, Low temperature luminescence of $ZnMoO_4$ single crystals grown by low temperature gradient Czochralski technique. *Opt. Mater.* 34 (2012) 1804－1810

[9] L.Y. Zhou, J.S. Wei, F.Z. Gong, J.L. Huang, L.H. Yi, A potential red phosphor $ZnMoO_4:Eu^{3+}$ for light-emitting diode application. *J. Solid State Chem.* 181 (2008) 1337－1341.

[10] A. Xie, X. Yuan, F. Wang, Y. Shi, Z. Mu, Enhanced red emission in $ZnMoO_4:Eu^{3+}$ by charge compensation. *J. Phys. D － Appl. Phys.* 43 (2010) 055101.

[11] T. Chengaiah, C.K. Jayasankar, K. Pavani, T. Sasikala, L. Rama Moorthy, Preparation and luminescence characterization of $Zn(1-x)MoO_4$: xDy^{3+} phosphor for white light-emitting diodes.

Opt. Commun. 312 (2014) 233－237.

[12] X. Ju, X. Li, W. Li, W. Yang, C. Tao, Luminescence properties of $ZnMoO_4$:Tb^{3+} green phosphor prepared via co-precipitation. *Mater. Lett.* 65 (2011) 2642－2644.

[13] C. Peng, L. Gao, S.W. Yang, J. Sun, A general precipitation strategy for large-scale synthesis of molybdate nanostructures. *Chem. Commun.* 43 (2008) 5601－5603.

[14] G.K. Zhang, S.J. Yu, Y.Q. Yang, W. Jiang, S.M. Zhang, B.B. Huang, Synthesis, morphology and phase transition of the zinc molybdates $ZnMoO_4 \cdot 0.8H_2O$/ α -$ZnMoO_4$/$ZnMoO_4$ by hydrothermal method. *J. Cryst. Growth* 312 (2010) 1866－1874.

[15] L.X. Yu, M. Nogami, The synthesis and photoluminescent properties of one-dimensional $ZnMoO_4$:Eu^{3+} nanocrystals. *Mater. Lett.* 64 (2010) 1644－1646.

[16] Y. Keereeta, T. Thongtem, S. Thongtem, Characterization of $ZnMoO_4$ nanofibers synthesized by electrospinning-calcination combinations. *Mater. Lett.* 68 (2012) 265－268.

[17] J.H. Ryu, S.M. Koo, J.W. Yoon, C.S. Lim, K B. Shim, Synthesis of nanocrystalline $MMoO_4$ (M=Ni, Zn) phosphors via a citrate complex route assisted by microwave irradiation and their photoluminescence. *Mater. Lett.* 60 (2006) 1702－1705.

[18] Y. Liang, P. Liu, H.B. Li, G.W. Yang, $ZnMoO_4$ micro- and nanostructures synthesized by electrochemistry-assisted laser ablation in liquids and their optical properties. *Cryst. Growth Des.* 12 (2012) 4487－4493.

[19] D.A. Spassky, I.A. Kamenskikh, A.E. Savon, S.G. Nedilko, P.A. Lykov, Electronic structure and luminescence mechanisms in $ZnMoO_4$ crystals. *J. Phys. Condens. Mat.* 23 (2011) 365501.

[20] Y.M. Huang, Q.L. Ma, B.G. Zhai, A simple method to grow one-dimensional ZnO nanostructures in air. *Mater. Lett.* 93 (2013) 266－268.

[21] Y.M. Huang, Q.L Ma, B.G. Zhai, Controlled morphology of ZnO nanostructures by adjusting the zinc foil heating temperature in an air-filled box furnace. *Mater. Chem. Phys.* 147 (2014) 788－795.

[22] Q.L. Ma, R. Xiong, B.G. Zhai, Y.M. Huang, Ultrasonic synthesis of fern - like ZnO nanoleaves and their enhanced photocatalytic activity. *Appl. Surf. Sci.* 324 (2015) 842－848.

[23] Q.L. Ma, R. Xiong, B.G. Zhai, Y.M. Huang, Core-shelled Zn/ZnO microspheres synthesized by ultrasonic irradiation for photocatalytic applications. *Micro Nano Lett.* 8 (2013) 491－495.

[24] Y.M. Huang, Q.L. Ma, B.G. Zhai, Core-shell Zn/ZnO structures with improved photocatalytic properties synthesized by aqueous solution method. *Funct. Mater. Lett.* 6 (2013) 1350058.

[25] N.N. Solovev, M.L. Meiman, K.A. Kuvshinova, A.G. Smagin, V.G. Kozlov, Electron paramagnetic resonance and structure of crystals of zinc molybdate $ZnMoO_4$. *J. Struct. Chem.* 20 (1979) 377－384.